IEEE Access
Multidisciplinary ⋮ Rapid Review ⋮ Open Access Journal

Received 20 September 2022, accepted 21 October 2022, date of publication 26 October 2022, date of current version 2 November 2022.

Digital Object Identifier 10.1109/ACCESS.2022.3217476

RESEARCH ARTICLE

Mechanism Analysis and Multiphysics Validation of Lightning Attenuation in Constrained Space

YANG LU, JUFENG WANG, YANLEI WANG, AND PING HUANG
School of Electrical Engineering, Guangxi University, Nanning 530004, China

Corresponding author: Yang Lu (912522195@qq.com)

This work was supported by the Guangxi Innovation-Driven Development Project under Grant AA18242050.

ABSTRACT The problem of resistance reduction has always been the key and difficult point of lightning protection. However, the problem of reducing the grounding resistance efficiently has not been solved. A method is introduced in this paper to solve this problem from the lightning current attenuation. The lightning discharge shock wave mechanism, shock overpressure reflection mechanism, and arc truncation mechanism are included to theoretically analyze the lightning current attenuation mechanism. The overpressure of the lightning discharge is much higher than the cut-off arc radial tolerance pressure, which contributes to the temporarily closing of discharge channel. Moreover, a lightning discharge model is established in COMSOL to simulate the process of discharge in lightning current. The results show that the pressure in the tube reaches up to 4×10^8 Pa rapidly, and the velocity in the mouth of the tube could reach as high as 4200 m/s. Finally, the current attenuation experiments are designed to validate the lightning current attenuation effect. The results show that the current is attenuated by the action of the prototype, the amplitude of the impulse current decreased from 66.95 kA to 35.10 kA, and the steepness of the impulse current decreased from 18.49 kA/μs to 4.14 kA/μs. All of the results show that this method could efficiently attenuate lightning currents.

INDEX TERMS Grounding resistance, lightning current, lightning protection, current attenuation.

I. INTRODUCTION

The interruptions of the power supply system caused by lightning strikes, destructive weather, or equipment failure, whether it is instantaneous, momentary, temporary, or sustained, can cause disruption, damage, and downtime, from the domestic user up to the commercial user. Lightning may affect the performance of power lines by both direct and indirect effects where the transient high voltages may cause flashover on the electrical equipment on the power line [1]. In high voltage transmission systems, the backlash can seriously destroy the system stability [2]. Hence, installation of lightning rods on transmission towers considers as one of common measure to prevent direct lightning strikes [3]. Besides, lightning towers have been installed around transmission corridors to prevent surrounding facilities being stroke by direct lightning [4]. [5], [6]. But the series of problems arising from the ground network resistance limitation are not solved.

The potential difference in the grounding grid generated by a lightning strike on the grounding grid can be expressed as [6] and [7]:

$$U = Ri + L\frac{di}{dt} \tag{1}$$

where R is the impulse grounding resistance of the grid, L is its inductance, and i is the lightning current. Equation (1) demonstrates that both the amplitude and steepness of the lightning current have influence in the potential difference of the grounding grid. The potential difference rise caused by lightning may reach up to tens of kilovolts, even can reach hundreds of kilovolts [9], [10]. Such a high increase in ground potential will certainly lead to grounding grid backlash. Hence, the grounding grid resistance must be restricted to lower levels. But it is restricted by cultivated land vegetation, road construction, and land acquisition compensation costs, the grounding electrode extension method is not

The associate editor coordinating the review of this manuscript and approving it for publication was Ali Raza.

applicable for grounding resistance reduction [11]. Besides, in order to reduce the grounding resistance, researchers have taken a series of measures, including increasing the depth of buried ground network, deep well grounding, local soil replacement and other technologies, but it is difficult to achieve the requirements of grounding resistance [8], [12], [13], [14], [15]. The lightning potential difference is also an uncontrollable quantity, since the resistance is undefined [16]. In other words, the lightning grounding potential less than the insulation strength might be an uncertainty factor can cause serious failure for the power system.

Excessive ground potential is easy to make the substation primary equipment in the weakest resistance to the low-voltage lightning arrester suffered damage [17]. Due to the high-frequency characteristics of the lightning current and the longitudinal inductance of the grounding, the lightning current is mostly concentrated near the flash point, which results in uneven distribution of the ground network potential. These may lead to high ground potential, large step voltage and contact voltage, and potential risk of equipment and personnel exposure near the flash point [17], [18]. Studies have shown that a ground potential rise of 3.0 V will end up with a range of more than 4.0 km affect, and higher grounding resistance increases the range of influence of the grounding pole on surrounding facilities [5]. The ground potential rise caused by lightning strike may have wider impact area, which may have influence on adjacent lines and building facilities and damage home appliances as an irreversible effect [9], [19].

Darwin Kok Lian Chia [20] pointed out that the most direct approach in alleviating the damaging consequences of lightning is to reduce its current. However, there is no effective method yet to address such damage efficiently [21]. While the lightning current attenuation method that has been introduced in this paper can convert the lightning discharge shock wave into lightning arc extinguishing energy to act on the discharge channel to achieve the blocking of the discharge channel and the attenuation of the lightning current. If the lightning current is attenuated, some of the problems caused by lightning will be solved. **Figure 1** is the 3D model of the prototype. It is sealed at the bottom and open at the top. And it can be installed directly on top of the lightning rod. **Figure 2** shows the installation of the prototype.

This paper introduced the arc truncation mechanism by analyzing the lightning discharge shock wave mechanism, the shock overpressure reflection mechanism. And the COMSOL simulation is involved for the validation of above-mentioned mechanism, feature, and lightning attenuation effect. Last but not the least, the current attenuation experiments are made to check the lightning attenuation effect.

II. LIGHTNING ATTENUATION MECHANISM ANALUSIS

A. LIGHTNING DISCHARGE OVERPRESSURE

The energy of lightning discharge $E(t)$ injects into the discharge channel, part of the energy converts into the arc plasma

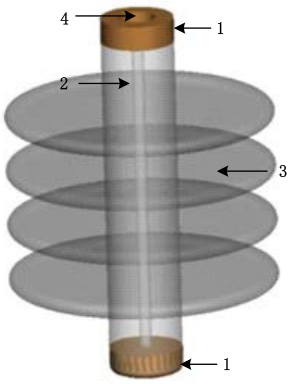

FIGURE 1. 3D model of the prototype: 1 is the metal electrode; 2 is rare earth tube wrapped by insulation material; 3 is insulation material; 4 is entrance of the lightning arc.

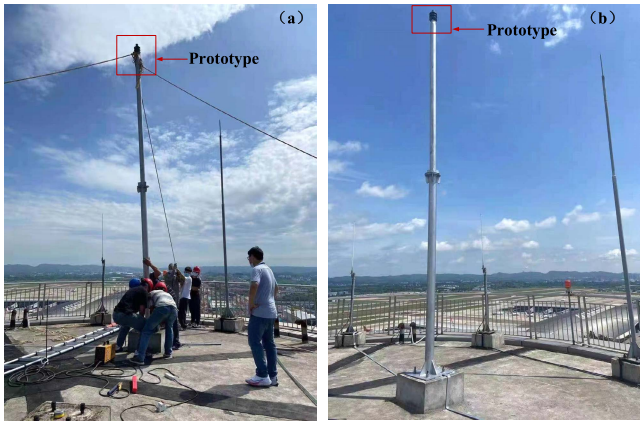

FIGURE 2. Installation of the prototype: (a) Installation site picture. (b) Actual operation picture.

energy $W(t)$, and another part of the energy converts into the energy consumption $M(t)$ for discharge channel expanding outward. The energy balance equation in the arc channel can be simplified as Equation (2):

$$M(t) + W(t) = E(t) = \int_0^t i^2(\tau) R_a d\tau \tag{2}$$

where i is the current of arc R_a is the resistance of the arc column channel. However, if assuming that the arc channel is cylindrical, the Equation (2) could be transformed into the form of an integral as indicated in Equation (3):

$$\frac{p(t)V(t)}{\gamma - 1} + \int_0^{t_0} p(r)\, 2\pi r l dr = \int_0^t i^2(\tau) R_a d\tau \tag{3}$$

where $p(t)$ is the pressure of the arc column channel; $V(t)$ is the volume of the arc column channel; γ is adiabatic index. The shock wave overpressure generated by the rapid expansion of the large current impulse discharge arc which can be written as Equation (4) [22]:

$$\Delta P = K_1 \rho_0 u_1^2 \tag{4}$$

In the Equation (4), $K_1 = 2(\gamma\text{-}1)/(\gamma\text{-}1)^2$, γ is isentropic adiabatic index of gas, for air $\gamma = 1.4$; ρ_0 is the initial gas density; u_1 is velocity of arc expansion. If taking Equation (4) into Equation (3), the differential form of the arc energy balance equation with respect to the radius r(t) will be obtained

as stated in Equation (5):

$$\frac{2\pi^2 K_1 \rho_0 \sigma_A}{\gamma - 1}\left(r^4 \frac{dr}{dt}\frac{d^2 r}{dt^2} + \gamma\left(r\frac{dr}{dt}\right)^3\right) = i^2 \tag{5}$$

If the arc channel radius can be further approximated as $r(t) = gt^k$. where g and k are coefficient to be determined, the energy balance equation can be simplified as Equation (6):

$$2\pi^2 K_1 \sigma_A \rho_0 \left(r\frac{dr}{dt}\right)^3 \left[1 + \frac{\left(\frac{d^2 r}{dt^2}\right)}{2\left(\frac{dr}{dt}\right)^2(\gamma - 1)}\right] = i^2 \tag{6}$$

By further converting $r(t) = gt^k$ into $k = \frac{t}{r}\frac{dr}{dt}$, and taking such replacement into Equation (7), Equation (8) is able to be obtained as well:

$$2\pi^2 K_1 \sigma_A \rho_0 \left(r\frac{dr}{dt}\right)^3 \xi = i^2 \tag{7}$$

$$\xi = 1 + \left(\frac{2 - k^{-1}}{\gamma - 1}\right) \tag{8}$$

It is assumed that the arc conductivity σ_A remains constant during the expansion of the arc channel, the arc channel radius expression can be derived as Equation (9) [11], [12]:

$$r(t) = \left(\frac{108}{125\pi^2 \rho_0 K_1 \sigma_A \xi}\right)^{\frac{1}{6}} i^{\frac{1}{3}} t^{\frac{1}{2}} \tag{9}$$

From Equation (10), it is able to conclude that $r(t)$ is proportional to $t^{5/6}$. Moreover, if Equation (9) is continuously derived, the expression of arc channel expansion rate can be obtained as Equation (10):

$$u(t) = \frac{dr}{dt} = \left(\frac{108}{125\pi^2 \rho_0 K_1 \sigma_A \xi}\right)^{\frac{1}{6}} \left(\frac{i^{\frac{1}{3}} t^{-\frac{1}{2}}}{2} + i^{-\frac{2}{3}} t^{\frac{1}{2}} \frac{di}{3dt}\right) \tag{10}$$

where arc conductivity $\sigma_A = 30000$ S/m; gas initial density $\rho_0 = 2.97$ kg/m^3.

Besides, the impulse arc current during wave-front time can also be written as (Equation (11)):

$$i = I_m\left(1 - e^{-\frac{t}{\tau_2}}\right) \tag{11}$$

The relationship between the wavefront time and wave-front time constant is Equation (12):

$$\tau_2 = \frac{0.6T_1}{In7} \tag{12}$$

The wavefront time T_1 is set to be 4 μs and the wavefront time constant τ_2 is 1.25 μs.

Taking Equation (11) and Equation (12) into Equation (10), and taking the result into Equation (4), the lightning arc impact overpressure curve is plotted. The different current lightning discharge overpressure curve under natural condition is shown in **Figure 3**.

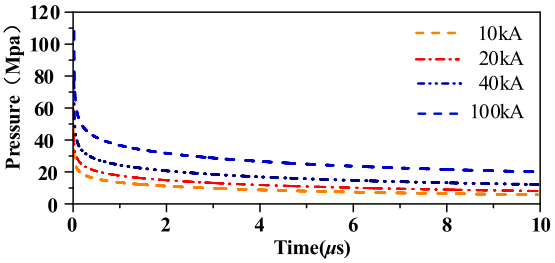

FIGURE 3. Different current lightning discharge overpressure curve under natural condition.

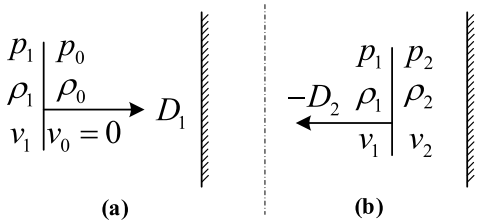

FIGURE 4. Positive reflection of shock wave overpressure on a rigid wall.

B. OVERPRESSURE REFLECTION MECHANISM

Figure 4 shows the positive reflection of a shock wave on a rigid surface. When the shock wave encounters on a rigid wall, the velocity of the air mass at the wall surface suddenly changes to zero, making a sharp accumulation of finger points (in fluid mechanics called standing point). The pressure and density rise suddenly and reflect in the opposite direction to a certain extent. Because the wall is rigid, the air mass close to the wall is stationary before the reflection forms, so the air shock wave and the rigid wall collision occurred in the moment of reflection, which eventually produces the propagation speed D_2, and opposite direction reflected shock wave [23].

The basic relationship equations of shock wave are normally stated as below two equations:

$$v_1 - v_0 = \sqrt{(P_1 - P_0)\left(\frac{1}{\rho_0} - \frac{1}{\rho_1}\right)} \tag{13}$$

$$v_2 - v_1 = \sqrt{(P_2 - P_1)\left(\frac{1}{\rho_1} - \frac{1}{\rho_2}\right)} \tag{14}$$

As $v_0 = v_2 = 0$, from Equations (13) and (14), we can get:

$$(P_1 - P_0)\left(\frac{1}{\rho_0} - \frac{1}{\rho_1}\right) = (P_2 - P_1)\left(\frac{1}{\rho_1} - \frac{1}{\rho_2}\right) \tag{15}$$

Consider the adiabatic equation of the shock wave as summarized in Equations (16) and (17):

$$\frac{\rho_1}{\rho_0} = \frac{\frac{k+1}{k-1}\cdot\frac{P_1}{P_0} + 1}{\frac{k+1}{k-1} + \frac{P_1}{P_0}} \tag{16}$$

$$\frac{\rho_2}{\rho_1} = \frac{\frac{k+1}{k-1}\cdot\frac{P_2}{P_1} + 1}{\frac{k+1}{k-1} + \frac{P_2}{P_1}} \tag{17}$$

The incident overpressure is normally calculated by Equation (18):

$$\Delta P_1 = P_1 - P_0 \tag{18}$$

The reflected overpressure is similarly calculated by Equation (19):

$$\Delta P_2 = P_2 - P_0 \tag{19}$$

Once both Equation (19) and Equation (20) are taken into Equation (16) with the consideration of incident and reflected overpressure equations, the peak reflected wave overpressure is obtained as Equations (20):

$$\Delta P_2 = 2\Delta P_1 + \frac{(k+1)\,\Delta P_1^2}{(k-1)\,\Delta P_1 + 2kP_0} \tag{20}$$

For air $k = 1.4$, and the reflected wave peak overpressure can be written as Equations (21):

$$\Delta P_2 = 2\Delta P_1 + \frac{6\Delta P_1^2}{\Delta P_1 + 7P_0} \tag{21}$$

To conclude, the air shock wave in the rigid wall after the reflection of the reflected wave should be two to eight times of the incident wave. In the formation and expansion of the arc accompanied by gas dissociation, electrolysis, and other effects. However, such analysis above does not take into account this effect. If this factor is taken into account, the value of the $\Delta P_2/\Delta P_1$ is considered to be higher than current amount.

C. DISCHARGE CHANNEL CUT-OFF MECHANISM

The relationship between shock pressure and cut-off arc radial tolerance pressure impact is analyzed by comparing the cut-off pressure with the overpressure reflection pressure to determine whether the arc can be cut off [24].

Equations (22) demonstrates the radial distribution of current:

$$I = 2\pi \int_0^{\alpha} J_z(r) r dr \tag{22}$$

where α and r are the radii, I is the arc current, and J_z is the axial arc density that is constant. The definition of current density is $J_z = I/S$, where S is the cross-sectional area of the arc. Considering that the arc truncation time is tens of μs, the arc density can be approximated as a constant in such a short time.

The intensity of the angular magnetic field is defined as Equations (23):

$$B_\theta = \frac{1}{2}\mu_r J_z r \tag{23}$$

where μ_r is the magnetic conductivity of the medium. The volume force acting on the arc plasma is based on the calculation method of Equations (24):

$$F = J \times B = F_r = -\frac{1}{2}\mu_r J_z^2 r \tag{24}$$

where F is the radial volume force, and the negative sign represents the force is pointing inward along the radial direction. When the current density is constant, the radial pressure distribution of the arc body is given by Equations (26):

$$P(r) = \frac{\mu}{4} J_z^2(\alpha^2 - r^2) \tag{25}$$

where $J_z = I/\pi\alpha^2$. In the arc column, we have $\alpha = r$. By substituting $J_z = I/\pi r^2$ into equation (21), the axial pressure of the arc is obtained as Equations (26):

$$P_1 = \frac{\mu_r I^2}{4\pi^2 r^2} \tag{26}$$

The flow of plasma will generate the corresponding kinetic energy, it produces the corresponding pressure as Equations (28):

$$P_g = \frac{1}{2}\rho v^2 \tag{27}$$

where P_g is the plasma kinetic-energy pressure, ρ is the plasma density, and the v is the plasma speed. The total pressure P of the arc is calculated by Equations (28):

$$P = P_1 + P_g = \frac{\mu_r I^2}{4\pi^2 r^2} + \frac{1}{2}\rho v^2 \tag{28}$$

However, as the Pressure P_g is small compared to Pressure P_1, the pressure P_g can be ignored, and the pressure of the arc can be written as Equations (29):

$$P = \frac{\mu_r I^2}{4\pi^2 r^2} \tag{29}$$

where i is the arc current, and r is arc radius. Substituting Equation (11) into Equation (29), the arc axial truncation pressure can be obtained as a new equation, Equations (30):

$$P_B(t) = \frac{I_m^2(1 - e^{-\frac{t}{\tau_2}})}{4\pi^2 r^2} \times 10^{-7} \tag{30}$$

The currents I_m are taken as 10kA, 20kA, 40kA and 100kA, and the graphs in **Figure 5** are obtained:

After the comparison between **Figure 3** and **Figure 5**, it can be found that the overpressure of the lightning discharge P_1 is much higher than the cut-off arc radial tolerance pressure P_2. Under the action of the overpressure, the discharge channel would be cut off rapidly. **Figure 6** indicates that the overpressure is much higher than the cut-off pressure in 10kA impulse current, which satisfies the arc cut-off condition.

Moreover, the shock waves may also have a stacking effect, i.e., the shock wave is reflected on the rigid wall after the formation of the reflected wave to the middle of the tube propagation, superimpose inside the tube, obtain a lot of energy within a short period of time. Similar to the superposition of waves in water will lift the water to form a water column, the superposition of shock waves inside the tube will remove out of the medium inside the tube. This will enhance the arc cut-off effect. In the lightning discharge overpressure reflection cut off the arc and shock wave superimposed on the double action of clearing the conductive medium lightning discharge channel periodic conduction, shutdown, lightning discharge speed is slowed down, the lightning current is attenuated.

III. ARC MULTI-PHYSICS FIELD SIMULATION

A. ARC SIMULATION MODEL

The discharge process of electric arc is a process which involves multiple physical field coupling, and change of

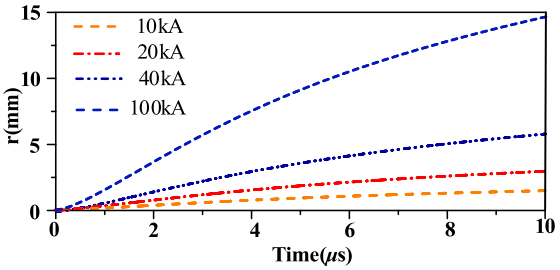

FIGURE 5. Pressure tolerance characteristics of arc truncation under different impulse current amplitude.

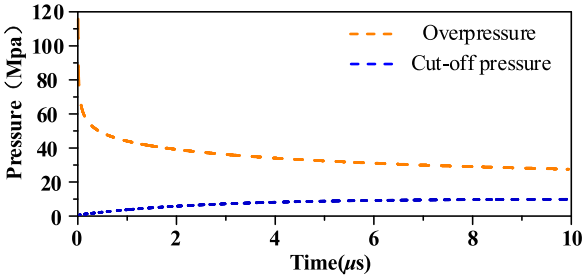

FIGURE 6. Pressure tolerance characteristics (satisfying arc cut-off condition).

field, including electric field, magnetic field, heat transfer field, fluid field, and many other multiple physical fields coupling. Such multi-physical field coupling may also lead to the relevant parameters between different physical fields interact. To simplify the model, the following assumptions are made [25]:

a) Arc plasma involved in this paper is a high heat and long arc plasma that satisfies the thermodynamic local thermodynamic equilibrium;

b) Thermal conductivity, kinetic viscosity, electrical conductivity, constant pressure heat capacity are all functions of temperature.

c) The arc is seen as a compressible flow in a laminar state (Ma < 0.3);

d) Arc density is the function of pressure and temperature.

According to the assumptions above, the arc plasma can be described by this model which satisfies the fluid characteristics described by the Navier-Stokes equation and electromagnetic field characteristics described by Maxwell equation, it mainly contains the following equations [26]:

First is the mass conservation equation (Equation (31)):

$$\frac{\partial \rho}{\partial t} + \nabla \cdot (\rho u) = 0 \tag{31}$$

where ρ is density of fluid, u is velocity vector.

Second is the energy conservation equation (Equation (32)):

$$\rho C_p \left(\frac{\partial T}{\partial t} + u \cdot \nabla T \right) = -(\nabla \cdot q) - \frac{T}{\rho} \cdot \frac{\partial \rho}{\partial T}|_p \left[\frac{\partial p}{\partial t} + (u \cdot \nabla) p \right] + Q \tag{32}$$

where C_{p} is constant pressure heat capacity, T is temperature of fluid, Q is plasma heat source, q is unit charge.

Third is the momentum conservation equation (Equation (33)):

$$\rho \frac{\partial u}{\partial t} + \rho (u \cdot \nabla) u = \nabla \cdot \left[-pI + \mu \nabla u + (\nabla u)^T - \frac{2}{3} \mu (\nabla \cdot u) I + F \right] \tag{33}$$

where p is pressure, I is unit matrix, μ is Dynami viscosity, F is Lorentz force.

In the COMSOL simulation platform, the Lorentz force is calculated using the magnetic vector potential. For the Lorentz force in the momentum equation, a volume force needs to be added under the flow field in order to realize the coupling the flow field and the magnetic field. The expression for the volume force is stated in (Equation (34)):

$$\begin{cases} F_x = B_{zmf} \times J_{ymf} - B_{ymf} \times J_{zmf} \\ F_y = -B_{zmf} \times mf \cdot J_{xmf} - B_{xmf} \times J_{zmf} \\ F_z = B_{ymf} \times mf \cdot J_{ymf} - B_{xmf} \times J_{ymf} \end{cases} \tag{34}$$

where $\boldsymbol{F}_{\mathbf{x,y,z}}$ is the component of the electromagnetic force in the right-angle coordinate system. While the magnetic field equation refers to Equation (35):

$$\begin{cases} \nabla \times H = J \\ E = -\dfrac{\partial A}{\partial t} \\ B = \nabla \times A \end{cases} \tag{35}$$

The current field equation may refer to Equation (36):

$$\begin{cases} \nabla \cdot \mathrm{J} = Q_{jv} \\ J = \delta E + \dfrac{\partial D}{\partial t} + J_e \\ E = -\nabla U \end{cases} \tag{36}$$

where J is current density, Q_{jv}.

Lastly, the gas state equation can refer to Equation (37):

$$p = \rho R T \tag{37}$$

where R is Gas constants, k is Heat transfer rate.

B. SIMULATION MODEL AND BOUNDARY CONDITION

Based on the simulation model above, we have built the simulation model in COMSOL Multiphysics field simulation platform. **Figure 7** is the simulation model. In this modelling method, seven observation points are set. Six internal observation points are fixed inside the tube and one external observation point is fixed outside. The observation points are numbered 1 to 7 from the bottom up. **Figure 8** is flow chart of the simulation. The simulation step length is set to 0.1 μs. The solver adopts full coupling solution. 10 kA 4/10 μs impulse current are applied in the High-voltage side. The impulse is generated by the RLC circuit which is built in the AC/DC module. The arc is formed between the High-voltage side and Grounding side at the beginning of the simulation.

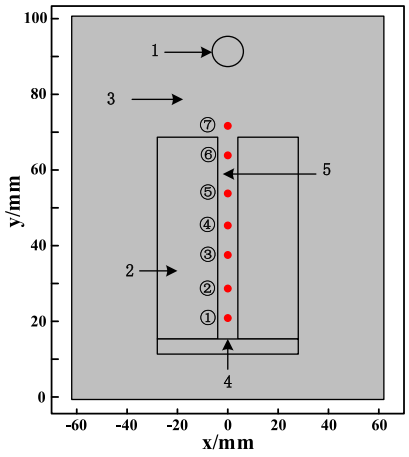

FIGURE 7. Simulation model for the prototype: 1 is the high voltage electrode; 2 is the insulating material; 3 is the air; 4 is the grounding electrode; 5 is the restraining pipe.

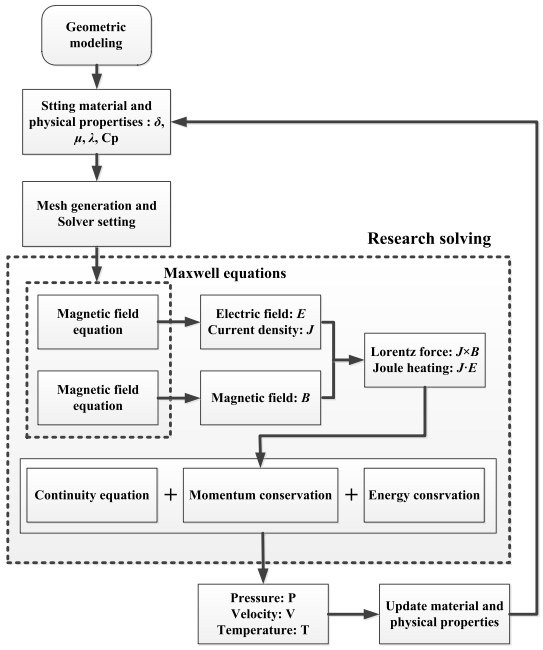

FIGURE 8. Flow chart of the simulation.

C. SIMULATION RESULTS AND ANALYSIS

The temperature change cloud of the simulation model with different impulse current are demonstrated correspondingly in **Figure 9**. At 0.1 μs, arc forms between high voltage electrode and ground. At this time, the temperature inside the tube is higher than outside the tube. It can be seen that there is a tendency for the energy mass surging out of the tube. At 1.0 μs, the energy mass has already surged out. The energy mass forms an umbrella-shaped high-temperature region outside the tube. With the development of discharge, the energy mass will spurt out more and more violently. At 2.0 μs, the energy mass is ejected to reach the high voltage electrode and expands around it. When it goes up to 4.0 μs, jet is sure to reach its intense state. After this, the jet is gradually diminishing. As shown in **Figure 9(e)** and **Figure 9(f)**, the jet has weakened. Through the temperature cloud, it can be found that the high-energy conductive medium inside the tube is ejected during the discharge. This is also consistent with the previous analysis, the high pressure formed inside the tube is able to discharge the conductive medium outside the tube. As shown in **Figure 9(g)** and **Figure 9(h)**, although lightning discharge has ended theoretical, the arc discharge does not finish. At 40.0 μs, the arc is just about to extinguish. At 50.0 μs, the arc is eventually extinguished. The actual discharge time is much longer than the theoretical discharge time (10 μs).

Figure 10 illustrates the axial pressure change curve at the observation point. From the curve of pressure over time, it can be observed that the axial pressure inside the tube increases rapidly to 4×10^8Pa at the beginning of the arc formation. The huge pressure inside the tube will discharge the conductive medium out of the tube, which is consistent with the previous theoretical analysis. At the same time, pressure drop from the bottom of the pipe to the outlet of the pipe, and great pressure gap exists between inside and outside the pipe. **Figure 11** shows the velocity variation curve of the observation point. It can be concluded that a high velocity airflow is formed in the tube and at the tube outlet. The closer to the mouth of the tube the greater the velocity, which is the opposite of the pressure distribution, and also shows that the pressure difference is the reason for the high velocity airflow. The velocity in the outlet of the tube reaches 4200 m/s. High-speed airflow accelerates the diffusion and compounding of conductive particles, which helps to increase the effect of closing the discharge channel.

IV. EXPERIMENT VALIDATION

A. EXPERIMENTAL PLATFORM

As shown in **Figure 12**, the experiment circuit diagram is composed by High-voltage Charging Unit and Pulsed Charging Unit. In the High voltage Charging Unit, the mains power is stepped up through the transformer and transformed into DC through the rectification circuit to supply Pulsed Charging Unit. The main circuit of the Pulsed Charging Unit is RLC oscillation circuit. The capacitor series get the electric from the High-voltage and trigger the Gap Switch when the voltage of capacitor series reach to setting value. Electric energy store in the capacitor series release and form impulse current. The change of voltage and current are collected by the Resistor Divider and Rogwski Coil. The output current of the Pulsed Charging Unit can be up to 100 kA. And the wave front and wave tail of the impulse is 4.0 μs and 10.0 μs. The test equipment was produced by Shanghai Guantu Electric Co. The experimental steps are as follows:

1) **Expected experiment**. Remove the prototype and connect the high voltage side and the ground side. Then turn on the power switch to charge the Capacitor Series to the set voltage. After charging is completed, the Gap Switch is triggered to discharge the circuit. In this step, the expected current waveform is able to obtain.
2) **Attenuation experiment**. Install the prototype on the high voltage side and the ground side. The capacitor

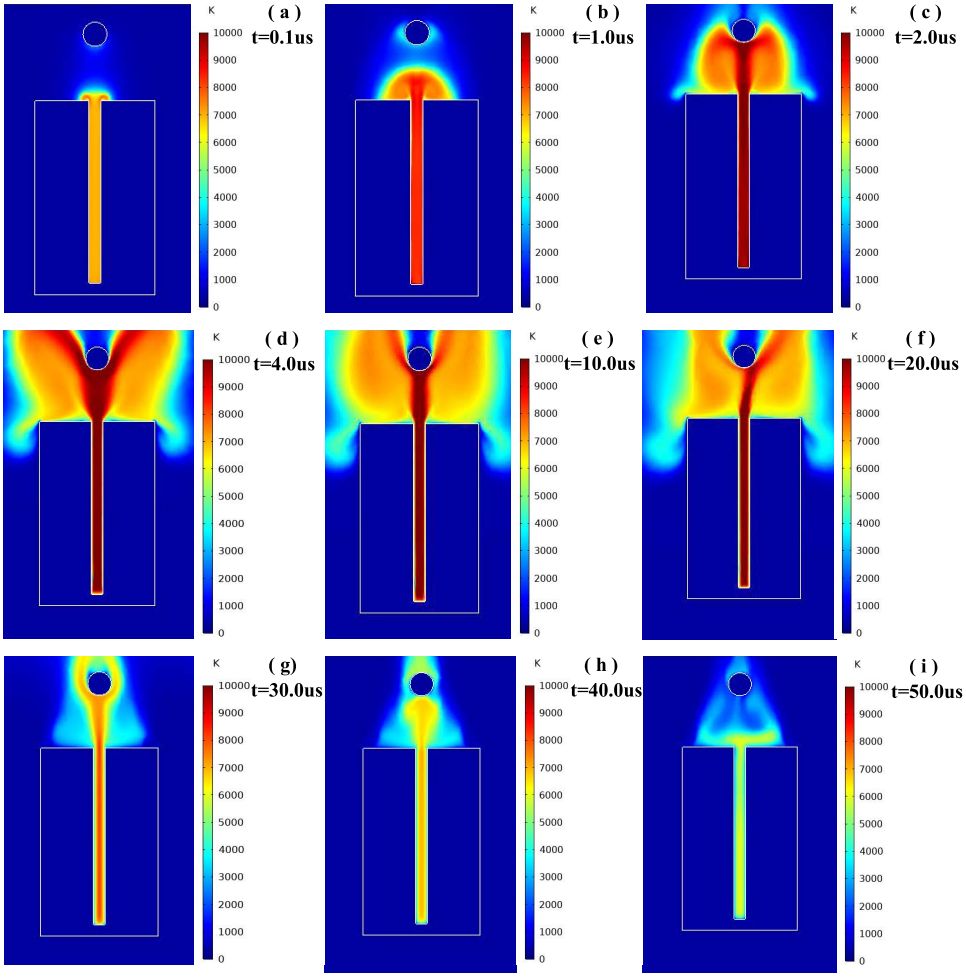

FIGURE 9. Temperature change cloud with different impulse current.

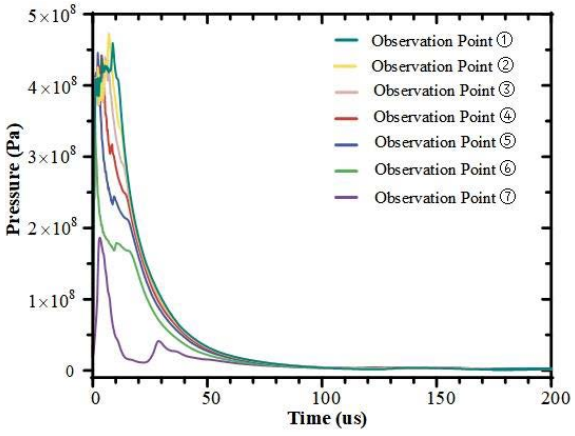

FIGURE 10. Pressure variation curve of each observation point.

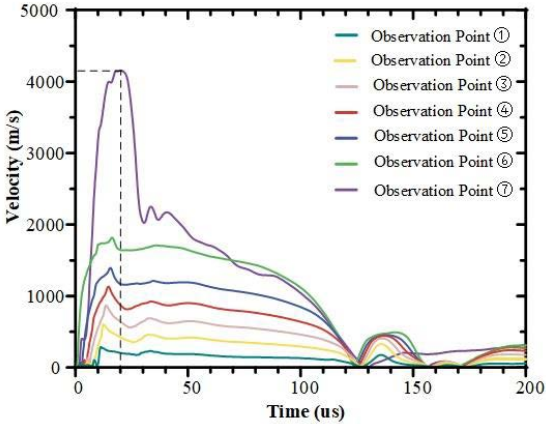

FIGURE 11. Velocity variation curve of each observation point.

is charged to the same voltage value as in step 3 and trigger the Gap Switch. In this step, the attenuation current waveform can be obtained as well.

B. VALIDATION RESULT AND ANALYSIS

The expected current without test prototype action is shown in **Figure 13(a)**, with a current amplitude of 66.95 kA, a wave-front time (T_1) of 3.62 μs, a wave-tail time (T_2) of 10.22 μs, and a wave-front steepness (di/dt) is 18.49 kA/μs. The current waveforms under the action of the test prototype are shown in **Figure 13(b)**. When the teat prototype is used, the current amplitude is 35.1kA, the wave-front time (T_1) is 8.47 μs, the wave-tail time (T_2) is 25.200 μs, and the wave-front steepness (di/dt) is 4.14 kA/μs.

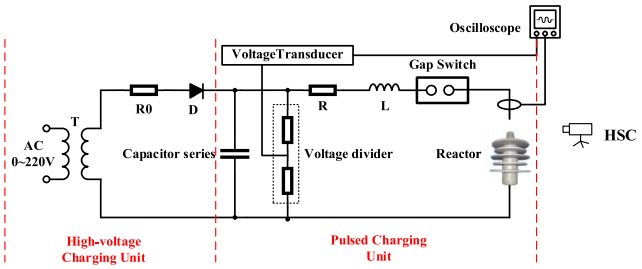

FIGURE 12. Schematic diagram of experimental circuit.

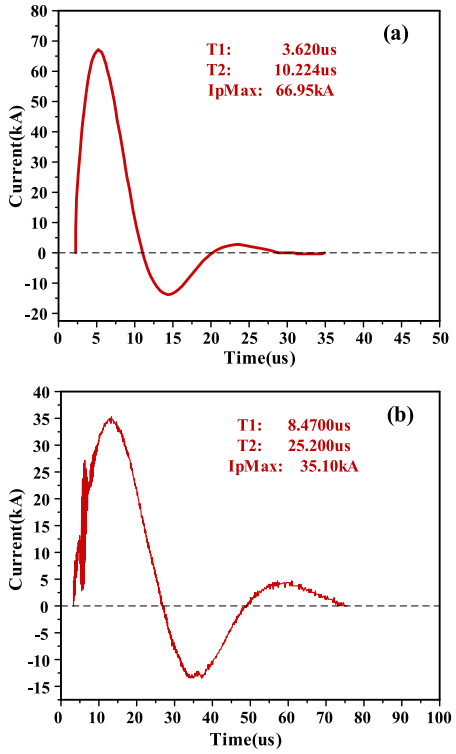

FIGURE 13. Impulse current waveform: (a) without prototype. (b) with prototype.

Compare the two waveforms, the wave-front time is found to be at 3.62 μs without the action of the prototype, and that with the action of the prototype is 8.47 μs. The latter is 2.3 times of former. The wave-tail time is 10.22 μs without the action of the prototype, and that with the action of the prototype is 25.20 μs. The latter is 2.5 times of the former. The latter current amplitude becomes 50 % of the former, and the latter current wavefront steepness becomes 20 % of the former. The second waveform shows a large vibration at the wavefront position.

The amount of charge corresponding to the two discharge current waveforms are also calculated based on Equation (38):

$$Q = \int_{t_1}^{t_2} idt = \sum_{n=1}^{M} \Delta t \cdot i_n \tag{38}$$

where t_1 indicates the beginning moment of current, t_2 indicates the end moment of current, M indicates discharge time equivalent fraction, i_n indicates the discrete current, and $\Delta t = (t_2\text{-}t_1)/M$. By calculation, the first waveform corresponds to the amount of discharge charge $Q_1 = 0.292C$, the second waveform corresponds to the amount of discharge charge $Q_2 = 0.297C$. Q_1 and Q_2 are essentially equal. Therefore, it can be assumed that the current is attenuated under the action of the prototype.

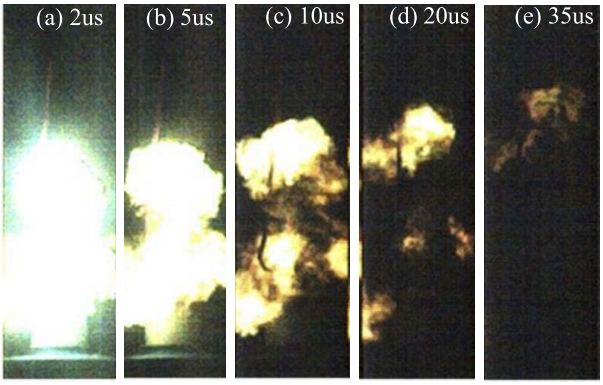

FIGURE 14. High-speed photography photos of the experiment.

High-speed photography photos of the experiment is also demonstrated in **Figure 14**. As shown in **Figure 14(a)** and **Figure 14(b)**, discharge channel forms, the arc is driven out of the prototype which means that shock overpressure removes the conductive medium to the outside of the tube. It is time to 10 μs (**Figure 14(c)**), the jet weakens. **Figure 14(e)** shows that the discharge has ended. The motion characteristics of the arc in the experiment are generally consistent with those in the simulation. This is consistent with the simulation results.

V. CONCLUSION

- Under the action of the device, the lightning energy is transformed into the truncated energy of the lightning discharge channel, turning the lightning fast and continuous discharge process into a slow and intermittent discharge process. Experiment shows that the lightning current was significantly attenuated in the action of prototype, the amplitude of lightning current attenuated about 50%, and its steepness attenuated about 70%. The simulation shows that a high-speed airflow with speed of 4200 m/s would form and the axial pressure inside the tube increases rapidly to 4×10^8 Pa at the beginning of the arc formation. This will help to increase the cut-off effect of the arc channel.
- The prototype could significantly reduce the potential difference caused by lightning strike in high soil resistivity areas, and notably decrease the cost of lightning protection. And it only needs to be installed on top of the existing lightning rod, which can save retrofitting costs.
- In this paper, we just studied single pulse attenuation effect. Future research should consider the multiple lightning strikes and other safety issues.

ACKNOWLEDGMENT

The authors would like to thank all the researchers at the High-Voltage Laboratory of Guangxi University.

REFERENCES

[1] R. Zeng, C. Zhuang, X. Zhou, S. Chen, Z. Wang, Z. Yu, and J. He, "Survey of recent progress on lightning and lightning protection research," *High Voltage*, vol. 1, no. 1, pp. 2–10, 2016.

[2] W. Li, L. Liu, L. Sun, J. Hu, J. Wang, and Y. Xie, "Analysis and countermeasures of the tilt of lightning rod in transformer substation," in *Proc. IOP Conf., Earth Environ. Sci.*, 2019, vol. 358, no. 4, Art. no. 042073.

[3] L. Cai, J. Li, R. Su, M. Zhou, Z. Xu, Q. Li, and J. Wang, "Rocket-triggered-lightning strikes to 10 kV power distribution lines and associated measured parameters of lightning current," *IEEE Trans. Electromagn. Compat.*, vol. 64, no. 2, pp. 456–463, Apr. 2022.

[4] X. Peng, Z. Deng, Y. Wang, R. Wang, M. Zhang, and X. Yang, "Effect evaluation of active lightning protection and regional lightning protection of power transmission lines based on triggering lightning tower array," *High Voltage Eng.*, vol. 48, no. 3, pp. 1077–1088, 2022.

[5] L. Xia, T. Zhou, B. Xu, and G. Wang, "Analysis of ground resistance limitation value of HVDC electrode system under high soil resistivity condition," *High Voltage Eng.*, vol. 47, no. 5, pp. 1720–1728, 2021.

[6] C. Li, K. Su, Y. Zhang, Z. Lu, and R. Wang, "Backflash simulation research on substation ground potential rise to low voltage arrester," *Insulators Surge Arresters*, vol. 4, pp. 178–183, Mar. 2020.

[7] Y. Chen, J. Wang, P. Huang, Y. Wang, and Y. Zhang, "Arc-extinguishing characteristics of semi-enclosed structures based on theory of positive shock wave reflection," *AIP Adv.*, vol. 12, no. 1, Jan. 2022, Art. no. 015009.

[8] D. Huang, J. Chen, S. Gu, C. Zhao, J. Ruan, and Z. Cui, "Characteristics of flexible graphite grounding material and its application in lightning protection," *High Voltage Eng.*, vol. 44, no. 6, pp. 1766–1773, 2018.

[9] K. Liu, S. Zhang, B. Li, C. Zhang, B. Liu, H. Jin, and J. Zhao, "Flexible grounding system for single-phase to ground faults in distribution networks: A systematic review of developments," *IEEE Trans. Power Del.*, vol. 37, no. 3, pp. 1640–1649, Jun. 2022.

[10] R.-F. Weng, X.-L. Bian, P. Long, Q.-Y. Cai, X. Guo, and W.-R. Si, "Simulation calculation of impulse grounding resistance of 10 kV distribution line, Part 3: Methods comparison and device development," in *Proc. 13th Int. Conf. Measuring Technol. Mechatronics Autom. (ICMTMA)*, Jan. 2021, pp. 118–126.

[11] Y. Hu, Z. Liu, T. Huang, Y. An, W. Shen, S. Hu, C. Ma, B. An, and D. Chen, "A new grounding resistance reduction method for wind turbines by grounding grid connection in limited areas," *Frontiers Energy Res.*, vol. 10, p. 375, Mar. 2022.

[12] R. Zeng, P. Zhou, S. Wang, Z. Li, and B. Zhang, "Field test on the reducing resistance natural of grounding module and building of its simulation model," *High Voltage Eng.*, vol. 36, no. 9, pp. 2112–2119, 2010.

[13] W. Liu, Y. Qiu, and L. Sun, "Research on resistance reducing scheme optimization of 500 kV transmission line tower grounding grid in different environments," *Power Syst. Protection Control*, vol. 46, no. 13, pp. 98–106, 2018.

[14] L. Zhou, X. Li, Q. Lv, Z. Xiang, S. Liu, and J. Ai, "Research on the efficiency and influence factors of resistance reducing agent in transmission line grounding grid," in *Proc. 4th Int. Conf. Intell. Green Building Smart Grid (IGBSG)*, Piscataway, NJ, USA, Sep. 2019, pp. 76–81.

[15] H. Xie, F. Yang, M. Hua, S. Liu, J. Hu, and Y. He, "Grounding grid corrosion detection based on mini-batch gradient descent and greedy method," *AIP Adv.*, vol. 11, no. 6, Jun. 2021, Art. no. 065034.

[16] R. Zeng, X. Zhou, and Z. H. Wang, "Review of research advances and fronts on international lightning and protection," *High Voltage Eng.*, vol. 41, no. 1, pp. 1–13, Jan. 2015.

[17] H. Chen, J. Huang, S. Yang, Q. Li, X. Yang, and W. Zhou, "Experimental investigation on impulse characteristics of grounding grid in substation," *High Voltage Eng.*, vol. 44, no. 5, pp. 1619–1626, 2018.

[18] S. Xie, R. Zeng, J. Li, C. Zhuang, Y. Zhang, and S. Chen, "Simulation on the characteristics and its influence factors of lightning intruding wave in substation," *High Voltage Eng.*, vol. 42, no. 5, pp. 1556–1564, 2016.

[19] A. Taher, A. Said, T. Eliyan, and A. Hafez, "Analysis and mitigation of ground grid lightning potential rise," *Trans. Electr. Electron. Mater.*, vol. 21, no. 3, pp. 305–314, Jun. 2020.

[20] D. K. L. Chia and A. C. Liew, "Analysis of effect of resistive lightning protection terminal on lightning return stroke current," *IEEE Trans. Power Del.*, vol. 20, no. 3, pp. 2307–2314, Jul. 2005.

[21] Y. Han, J. Zhang, Y. Ruan, L. Tang, D. Dai, and L. Li, "Mechanism of improving the lighting protection performance of back-flashover due to inductive lightning rod," *High Voltage Eng.*, vol. 42, no. 11, pp. 3456–3463, 2016.

[22] J. Xiong, L. Li, H. Dai, H. Wu, and M. Peng, "Analysis of shock wave overpressure effect of high current impulse arcs based on the explosive wave and energy balance theory," *Proc. CSEE*, vol. 38, no. 22, pp. 6746–6753, 2018.

[23] S. Lin, J. Wang, T. Ma, J. Qin, H. Li, R. Huang, and L. Liu, "Superimposed effect of shock waves of underwater explosion," *Acta Armamentarii*, vol. 41, no. S1, pp. 39–45, 2020.

[24] Y. Wang, P. Huang, Y. Luo, Y. Chen, and J. Wang, "Mechanism for truncating power-frequency continuation and reburning by means of a super-strong arc-extinguishing gas," *AIP Adv.*, vol. 11, no. 3, Mar. 2021, Art. no. 035323.

[25] Z. Li, J. Wang, X. Zhou, S. Huang, R. Yan, and Z. Xia, "Influence of chamber structure on arc quenching in multigap system," *High Voltage*, vol. 5, no. 3, pp. 313–318, Jun. 2020.

[26] S. Huang, J. Wang, Y. Xu, Z. Li, R. Yan, and Q. Zhang, "The effect of a multi-fracture compression airflow arc-extinguishing structure interrupting the power frequency follow current," *AIP Adv.*, vol. 10, no. 3, Mar. 2020, Art. no. 035129.

YANG LU received the B.S. degree in electrical engineering and its automation from Jiangsu University, China, in 2020. He is currently pursuing the master's degree with Guangxi University, Nanning, China. His research interests include high voltage technology and modern lightning protection technology.

JUFENG WANG received the M.Sc. and Ph.D. degrees in high voltage engineering from Wuhan Electric Power University, Wuhan, China. He is currently a Professor with the School of Electrical Engineering, Guangxi University, Nanning, China. His research interests include basic theory and engineering applications of lightning protection in power grids.

YANLEI WANG received the Ph.D. degree in electrical engineering from Guangxi University, Nanning, China, in 2022. Her research interests include arc extinguishing and lightning protection.

PING HUANG received the M.S. and Ph.D. degrees in electrical engineering from Guangxi University, Nanning, China, in 2005 and 2018, respectively. She is currently an Assistant Professor with the School of Electrical Engineering, Guangxi University. Her current research interests include lightning protection of electrical insulation, gas discharge simulation, and parameter optimization.